1992-01-15

Observation of soft-x-ray spatial coherence from resonance transition radiation

Piestrup, M. A.

American Physical Society

Physical Review A, v. 45, no. 2, January 15, 1992, pp. 1183-1196
http://hdl.handle.net/10945/47500

Observation of soft-x-ray spatial coherence from resonance transition radiation

M. A. Piestrup, D. G. Boyers, C. I. Pincus, and Qiang Li
Adelphi Technology Inc., 285 Hamilton Avenue, Suite 430, Palo Alto, California 94301

G. D. Hallewell
Stanford Linear Accelerator Center, Stanford University, Stanford, California 94309

M. J. Moran
Lawrence Livermore National Laboratory, University of California, Livermore, California 94550

D. M. Skopik and R. M. Silzer
Saskatchewan Accelerator Laboratory, University of Saskatchewan, Saskatoon, Saskatchewan, Canada S7N 0W0

X. K. Maruyama and D. D. Snyder
Naval Postgraduate School, Monterey, California 93943

G. B. Rothbart
Software Science, Inc., 100 Valley Drive, Brisbane, California 94005
(Received 29 April 1991)

We have observed the spatial distribution of coherent or resonance transition radiation (RTR) in the soft-x-ray region of the spectrum (1–3 keV). Resonance transition radiators were constructed and tested at two accelerators using electron-beam energies ranging from 50 to 228 MeV. These radiators emitted soft x rays in a circularly symmetrical annulus with a half-angle divergence of 2.5–9.0 mrad. The angle of peak emission was found to increase with electron-beam energy, in contrast to the incoherent case, for which the angle of emission varied inversely with electron-beam energy. By careful selection of foil thickness and spacing, one may design radiators whose angle of emission varies over a range of charged-particle energies. A particular RTR mode ($r=m=1$) was found to give a sharp annular ring that becomes more accentuated as the number of foils is increased. The RTR effect has application in particle detection, beam diagnostics, x-ray source brightness enhancement, and x-ray free-electron-laser emission.

PACS number(s): 41.70.+t, 78.70.−g, 07.85.+n, 29.40.−n

I. INTRODUCTION

The generation of coherent x rays was first proposed by Ginzburg and Frank [1]. Garibyan and Ter-Mikaelian performed early theoretical calculations [2,3]. Transition radiation emitted from a single charged particle crossing a periodic medium where there is phase addition between the emitted photons at each interface was termed to be "resonant" by Ter-Mikaelian [3]. Fabjan and Struczinski [4] and others [5–8] have shown resonance by observing the photon-energy spectrum which was broken up into modes of smaller bandwidth. In an early experiment at the Lawrence Livermore National Laboratory (LLNL), we showed that phase coherence of ultrasoft x rays (150 eV) resulted in an unusual spatial interference pattern as predicted by resonance transition radiation [9]. In experiments presented here, we have observed the angular radiation pattern from coherent, or resonant, transition radiation (RTR) at soft-x-ray energies of 800 eV to 3 keV. Preliminary discussion of this work appeared previously [10,11]. The results showed clearly that we were observing coherency, and that the angle of emission increases with electron-beam energy. The latter is extremely important since it could form the basis of a new class of charged-particle detectors [10,11]. Goedtkindt *et al.* have recently performed similar experiments at higher electron-beam energies (500 MeV) with excellent results [12].

The measured spatial distributions presented here show strong interference in the soft-x-ray region generated by closely spaced foils (4–48 μm). X rays of this energy interfere in the radiators because of the relativistic contraction of the 50- to 220-MeV electrons, which reduces the effective foil spacing by a factor of 10^4 to 5×10^4. This interference shows that the x rays are generated coherently by the entire radiator structure. The radiation is termed coherent because the x rays generated are a simultaneous response of the entire radiator structure to each incident electron [9].

Phase coherence was shown by two methods. First, we were able to change the angle of peak emission by varying the foil thickness and spacing. This angle could be made to be less than or greater than the angle of peak emission for the incoherent radiator (randomly spaced foils), which is primarily a function of the emitting charged particle's energy. We were also able to change the angle

by rotating the stack in the beam around an axis perpendicular to the electron-beam direction [10].

Second, we were also able to show coherence by demonstrating a distinct functional difference in the angle of peak emission of x rays produced from a coherent radiator as opposed to an incoherent radiator. The angle of peak emission increased with increasing electron-beam energy for a coherent radiator, while the angle decreased for an incoherent radiator.

In addition, the spatial power distribution of the $r=m=1$ mode has a distinctive shape quite different from the incoherent case. Starting from the center of the annulus and moving radially, the power density has a slow rise, terminating at a peak with a sudden drop. This distinctive "cup shape" is quite different from the slow rise and fall of the incoherent mode. The complete $r=m=1$ resonance transition spatial distribution is shown here for the first time in both a three-dimensional fishnet plot and in a false-color display.

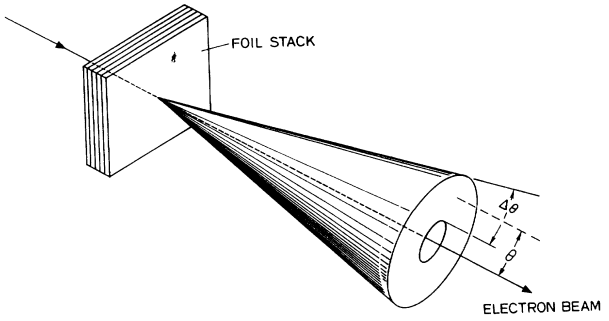

FIG. 1. A schematic diagram of the cone of emission produced by transition radiation showing the peak-emission angle and range of emission angles $\Delta\theta$. The coherent x rays are emitted in a small forward cone whose apex angle is dependent upon the foil spacing, foil thickness, foil material, and charged-particle energy.

II. THEORY

A. Determination of the photon spatial and spectral distributions

Transition radiation occurs when a moving charged particle encounters a sudden change in dielectric constant, such as occurs at an interface between two media (or between a vacuum and a medium) [1–3,13–15]. Ordinarily, a particle which is moving with constant velocity does not radiate unless the particle velocity equals the phase velocity of the emitted wave along the direction of particle motion, as in the case of Cherenkov radiation. However, if the interaction length is limited, or equivalently, if the dielectric constant is suddenly changed, as at the interface between two media, then velocity matching is not necessary. The minimum distance over which an electromagnetic wave and a charged particle can exchange energy is called the formation length, and is given by [13]

$$z_i(i=1,2)=\frac{2c}{\omega[1-\beta(\epsilon_i-\sin^2\theta)^{1/2}]}$$
$$\simeq\frac{4\chi\beta}{(1/\gamma)^2+\theta^2+(\omega_i/\omega)^2} \quad (1)$$

where $\gamma=(1-\beta^2)^{-1/2}$, $\epsilon_i=1-(\omega_i/\omega)^2$ are the permittivities of the two media, ω_i are their respective plasma frequencies, $\beta=v/c$, v is the speed of the electron, c the speed of light, $\chi=c/\omega$, and θ is the angle of emission. Thus there is emission at the interface if the material thickness on both sides of the interface is on the order of z_1 and z_2 or greater.

Emission can also occur for multiple interfaces such as between foils whose thicknesses are on the order of z_2 interspersed in a vacuum with separation on the order of z_1. These interfaces can be randomly spaced, as in foam plastic, or periodically spaced. As shown diagrammatically in Fig. 1, the x rays are emitted conically in an annulus whose apex angle of emission is $\theta_s\simeq 1/\gamma$ when there is no phase addition between foils.

The differential cross section for transition radiation production per photon-energy interval per solid angle is given by an expression of the form [4,13]

$$\frac{d^2N(\omega)}{d\omega d\Omega}=F_1F_2F_3\ , \quad (2)$$

where $N(\omega)$ is the number of photons and ω is their radial frequency.

The first factor F_1 is the contribution from a single interface and is given by [13]

$$F_1=\frac{\alpha\omega\sin^2\theta}{16\pi^2c^2}(z_1-z_2)^2\ , \quad (3)$$

where $\alpha=\frac{1}{137}$ is the fine-structure constant.

There is an angle that maximizes the radiation F_1 from a single interface. For the conditions $\theta^2\ll 1$, $\epsilon_i\simeq 1$, and $\beta\simeq 1$, this optimizing angle is [14]

$$\theta_s^2=\tfrac{1}{3}\{-(\delta_1+\delta_2)+[(\delta_1+\delta_2)^2+12\delta_1\delta_2]^{1/2}\} \quad (4a)$$

where $\delta_i=1/2\gamma^2+\omega_i^2/2\omega^2$. A first-order approximation is

$$\theta_s\simeq\left[\frac{1}{\gamma^2}+\left[\frac{\omega_1}{\omega}\right]^2\right]^{1/2} \quad (4b)$$

where ω_1 is the plasma frequency of the interfoil gas. If there is a vacuum between the foils, then $\omega_1=0$ and $\theta_s\simeq 1/\gamma$. There may be considerable intensity, however, up to the angle [13]

$$\theta_m\simeq\left[\frac{1}{\gamma^2}+\left[\frac{\omega_2}{\omega}\right]^2\right]^{1/2} \quad (5)$$

where ω_2 is the plasma frequency for the foils.

The second factor F_2 accounts for the coherent superposition of radiation from the two surfaces of a single foil. If the incoherent effects of electron collisions within the foil and the photon attenuation through the foil are ignored, F_2 assumes the familiar two-source interference pattern

$$F_2 = 4\sin^2\left[\frac{l_2}{z_2}\right], \tag{6}$$

where l_2 is the thickness of the foil. The factor-of-4 increase in peak intensity is the most striking manifestation of the two-surface constructive interference.

The third factor F_3 describes the summation of contributions from each foil in the stack. Again, there is a superposition of M (the number of foils) coherent sources. In its simplest form,

$$F_3 = \frac{\sin^2 MX}{\sin^2 X}, \tag{7}$$

where $X = (l_1/z_1) + (l_2/z_2)$.

In the case of a periodic medium, an $r\pi$ phase slippage is the condition for constructive interference or resonance between foil interfaces. If the foil thicknesses are not z_1 and z_2, the maximum energy exchange and resonance occur when

$$X = \frac{l_1}{z_1} + \frac{l_2}{z_2} = r\pi, \tag{8a}$$

$$\frac{l_2}{z_2} = (m - 1/2)\pi \tag{8b}$$

where r and m are positive integers. Using these values for l_1 and l_2, Eq. (2) becomes

$$\frac{d^2N}{d\Omega d\omega} = 4M^2 F_1 . \tag{9}$$

Equations (8a) and (8b) are the coherence conditions, i.e., the requirements for in-phase addition of the radiation from all interfaces. To minimize photon absorption and electron scattering, l_1 should be as small as possible, which means choosing $r = m = 1$. For those values,

$$l_{1,2} = \left[\frac{\pi}{2}\right] z_{1,2} . \tag{10}$$

Substituting into Eq. (8a) expressions for z_1 and z_2 and solving for $\cos\theta$, we obtain

$$\cos\theta_r = \frac{l_1 + l_2}{l_1(\epsilon_1)^{1/2} + l_2(\epsilon_2)^{1/2}} \left[\frac{1}{\beta} - \frac{r\lambda}{l_1 + l_2}\right] . \tag{11}$$

This is the resonance condition for transition radiation or the angle at which phase matching between waves can occur at each interface (Fig. 2) [3]. For small angles, Eq. (11) can be written as

$$\theta_r^2 = \frac{2r\lambda}{l} - \frac{1}{\gamma^2} - \left[\frac{\omega_0}{\omega}\right]^2 . \tag{12}$$

where $\omega_0^2 = (\omega_1^2 l_1 + \omega_2^2 l_2)/(l_1 + l_2)$ and $l = l_1 + l_2$.

From (11) and (12) we see that the angle of emission is determined by the foil thickness and the energy of the emitting particle. Thus, by measuring the angular positions of these modes, we can determine particle energy. We also note that θ_r can be greater than $1/\gamma$, which would allow the measurement of extremely relativistic electrons. Unlike the single interface angle of emission,

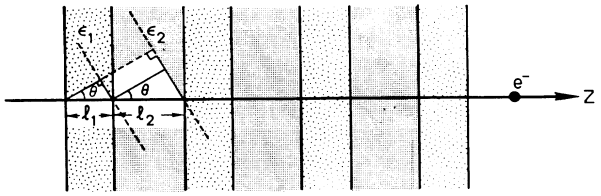

FIG. 2. Resonance transition radiation from a periodic medium with uniform spacing. If the phase velocity of the emitted radiation along the z direction slips out of phase by $2\pi r$ rad (r is an integer) for each foil pair interface, the radiation adds in phase and the intensity varies as square of the number of foils.

θ_r increases with electron-beam energy.

If the cumulative photon attenuation through the successive foils is included, then F_3 takes the form [4,16]

$$F_3 = \frac{1 + \exp(-M\sigma) - 2\exp(-M\sigma/2)\cos(2MX)}{1 + \exp(-\sigma) - 2\exp(-\sigma/2)\cos(2X)} \tag{13}$$

where $\sigma = \mu_1 l_1 + \mu_2 l_2$ and μ_i are the x-ray-absorption coefficients.

Random variation in the foil thicknesses and spacing will destroy coherency. Garibyan, Gerorgyan, and Yang have shown that if the variation in foil thicknesses and spacing satisfies the inequality [16,14,15]

$$2M\left[\frac{\Delta_1^2}{z_1^2} + \frac{\Delta_2^2}{z_2^2}\right] \ll 1 \tag{14}$$

where Δ_1 and Δ_2 are the standard deviations in foil dimensions, then it can be shown that for $M \gg 1$ and for the $r = m = 1$ case

$$\frac{l_1}{z_1} = \frac{l_2}{z_2} = \frac{\pi}{2} \tag{15}$$

then

$$\frac{d^2N}{d\Omega d\omega} \simeq 4M^2\left[1 - \frac{4M}{3}\left[\frac{\Delta_1^2}{z_1^2} + \frac{\Delta_2^2}{z_2^2}\right]\right]\frac{d^2N_0}{d\Omega d\omega} \tag{16}$$

where $l_{1,2}$ are the mean spacing and thickness. Thus, when Eq. (14) is satisfied, the reduction in emission from the ideal coherent case resulting from variations in thickness is small. An upper bound on the standard deviation of the thickness and spacing would be approximately

$$\Delta_1 \ll \frac{z_1}{\sqrt{2M}}, \tag{17a}$$

$$\Delta_2 \ll \frac{z_2}{\sqrt{2M}} . \tag{17b}$$

For example, in the case of the radiator described in Sec. IV, where $l_1 = 8.5$ μm, $l_2 = 3.5$ μm, and $M = 8$, the upper bounds on the standard deviations are $\Delta_2 \ll 0.6$ μm and $\Delta_1 \ll 1.4$ μm. These are not unreasonable mechanical tolerances. Thus we are able to construct periodic structures whose parameter accuracies are on the order of optical wavelengths and yet are "resonant" or coherent for soft-x-ray wavelengths.

Finally, if the distances l_1 or l_2 are random, or if the

angular and spectral structure associated with Eq. (13) cannot be resolved by the experiment, then Eq. (13) must be averaged over X. This yields

$$F_3 = \frac{1-\exp(-M\sigma)}{\sigma} . \quad (18)$$

This we will term the incoherent case.

For the incoherent stack, the angle of peak emission will follow that of the single interface angle of emission, θ_s, given by Eq. (4a) which varies roughly as $1/\gamma$. Thus, unlike the coherent case, as the electron-beam energy increases, the angle of peak emission decreases. As we increase the energy to ultrarelativistic values, θ_s becomes extremely small. For example, at 1 GeV, $\theta_s \simeq 0.5$ mrad; accordingly, obtaining the energy from the measurement of the cone angle becomes increasingly difficult for high-energy electron beams. However, for high-mass particles γ can remain small enough for relatively large angles, permitting the x-ray annulus to be imaged.

Two kinds of simulation routines were performed which calculate angular distributions and photon-energy spectrums. Integrating Eq. (2) over the bandwidth of the detector, one obtains the angular distribution of the photons. Integrating over the angular scan of the detector, one obtains the photon-energy spectrum. Integrations were done by the Simpson-rule method.

B. The fundamental resonance mode

As can be seen from Eqs. (11) and (12), a large number of r values or modes is possible. The resulting angular distribution from all these modes depends upon the number of foils and frequency band of emission. In some cases the distribution breaks up into a multiple-lobe pattern [9,10]. However, we can make the $r=1$ mode dominate by choosing $r=m=1$, and limiting the angle of peak emission to $0<\theta_r<\theta_m$. The angular distribution then shrinks inward to a single lobe, narrower than the angular distribution for the incoherent case. This is illustrated in Fig. 3 where the incoherent case is compared to the coherent case. Figure 3 was generated with the radiator parameters used in the experiment performed with the Naval Postgraduate School linac, discussed in Sec. IV. Measured results are shown in Fig. 12.

To obtain the $r=m=1$ mode we calculate l_1 and l_2 by substituting the desired θ and ω into Eq. (10). Knowing the absorption of the foil material, we then calculate the number of foils from $M<2/\mu l_2$. The mode thus selected is dominated by a single peak characteristic of the $r=m=1$ mode as shown in Fig. 3. As the number of foils is increased, the mode becomes more pronounced and peaked. The shape of the mode produced under these conditions is similar for other x-ray energies and has a universal shape when radiation is optimized near the angle of peak emission ($\theta_r=\theta_s\simeq 1/\gamma$ for the single-interface term [Eq. (3)]). The mode has a characteristic slow rise to the peak with a sudden fall off after θ_r. Figure 4 shows the calculated transition-radiation angular distribution for 300-MeV electrons for varying numbers of Mylar foils. As the number of foils increases, the angular peak becomes more pronounced, allowing better spatial resolution of the x-ray annulus from improved particle-energy determination.

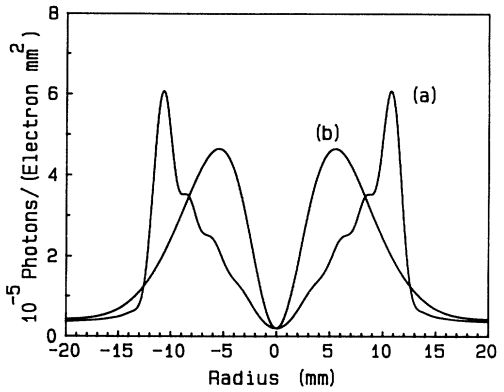

FIG. 3. The calculated angular distribution for the (a) coherent and (b) incoherent radiators. The stacks both have the same foil thickness and number, but with different spacing. The spacing for the incoherent stack is large ($\simeq 1.6$ mm) and random, while the spacing for the coherent case is small (4 μm) and periodic. The electron-beam energy is 98 MeV. The coherent stack consists of Mylar foils with $M=8$, $l_2=3.5$ μm, $l_1=4$ μm. The distance between the radiator and the detector is 1.34 m. See measured results in Fig. 12.

The desired frequency for resonance can be chosen between the high end of the spectrum, where the cutoff frequency is given approximately by $\omega_c \simeq \gamma\omega_p$, and the low end of the spectrum where absorption is so dominant that the number of foils that could be used is small. Designing the radiator to resonate at harder x-ray energies permits a large number of foils to be used. As an example, assuming an electron-beam energy of 300 MeV, we design three Mylar stacks to be resonant at 2, 4, and 6 keV, with

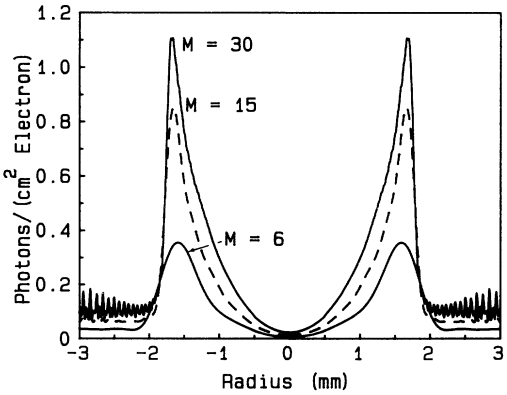

FIG. 4. The calculated spatial photon density as a function of radial distance from the axis of the electron beam from three Mylar-foil stacks with foil numbers of $M=6$, 15, and 30. The stacks were all designed to have peak emission at $\theta_r\simeq 1/\gamma=1.7$ mrad at 4 keV. The electron-beam energy is 300 MeV. The foil thickness and spacing for this design are $l_2=5.6$ μm and $l_1=16.4$ μm. The distance from the radiator to the detection plane is 1 m. As the number of foils increases, the peak of the annulus becomes more pronounced.

$\theta_r = \theta_s \simeq 1/\gamma = 1.7$ mrad. The spatial distributions and the parameters of the three stacks are given in Fig. 5. Note, the maximum number of foils ($M = 8$, 30, and 70) increases as the photon energy is increased. The radiation peak stays fixed as the photon energy and number of foils increase.

Figure 5 shows again the spatial distribution of the $r = m = 1$ mode to be characterized by a gradual rise to the peak followed by a rapid drop in flux. When the number of foils becomes large, the peak becomes sharper and higher-mode proliferation manifests in a rapid variation in intensity just below the peak [see Fig. 5(c)]. For finite electron-beam emittance, and detectors of finite area, this rapid variation in flux would not be observed [16].

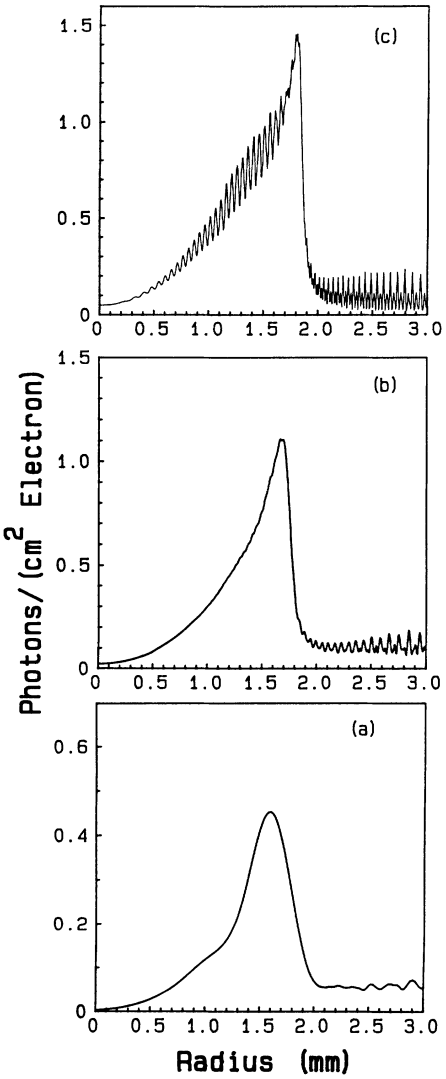

FIG. 5. The calculated spatial photon density for three RTR Mylar-foil radiators. The radiation is designed to peak at the same angle (1.7 mrad) but different photon energies (2, 4, 6 keV). The number of foils for each of the radiators increases with increasing photon energy. The parameters of each of the stacks are as follows: (a) $\omega = 2$ keV, $l_2 = 4.1$ μm, $l_1 = 107$ μm, $M = 8$; (b) $\omega = 4$ keV, $l_2 = 7.4$ μm, $l_1 = 53.4$ μm, $M = 30$; (c) $\omega = 6$ keV, $l_2 = 9.4$ μm, $l_1 = 35.6$ μm, $M = 70$. The electron-beam energy is 300 MeV. The distance from the radiator to the detector is 1 m; thus 1 mm represents 1 mrad on the x axis.

We can design foil stacks to be resonant at any desired angle between $0 < \theta_r < \theta_m$. For example, in Fig. 6 we show four x-ray spatial distributions which have been designed to peak at four different angles. The spatial photon density is plotted as a function of annulus radius. The distance between the radiator and the detector is 1 m, and the electron-beam energy is 300 MeV. The radiators are all designed to achieve resonance at 3 keV. Following the design procedure discussed above, we calculate the foil thickness l_2 and spacing l_1 assuming $\theta = 1$, 2, 4, and 8 mrad for each of the radiators. The stack parameters are given in the figure.

As can be seen from Fig. 6, the annular peaks appear to be maximum near $\theta_r = \theta_r \simeq 1/\gamma \simeq 1.7$ mrad. On either side of this maximum, the spatial photon density drops. However, the total number of photons in the annulus remains constant. The width of the annular peak grows with increasing radius or angle. Thus, for maximum ring image, setting $\theta_r = \theta_s \simeq 1/\gamma$ gives the high photon density in the ring annulus and, hence, the sharpest ring image.

The calculated spectra do not differ appreciably from what one obtains for incoherent stacks with small numbers of foils. Integrating Eq. (2) spatially, we obtain the spectral density as a function of photon energy. The calculated spectra generated by the Mylar foils used in two of the experiments discussed in Sec. IV are given in Fig. 7. The curve in 7(a) is the spectral density of x rays obtained from an eight-foil stack composed of 3.5-μm Mylar foils with vacuum spacing of 4.0 μm, while the curve in 7(b) is obtained from a four-foil stack composed of 2.5-μm Mylar foils separated by 35 μm. The electron-beam energy used for the eight-foil stack was 98 MeV, while that of the four-foil stack is 171 MeV. These pa-

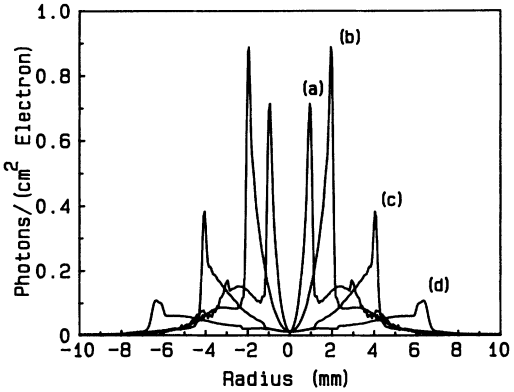

FIG. 6. The calculated spatial photon density for four RTR Mylar-foil radiators. The radiation is designed to peak at different angles (1, 2, 4, 8 mrad), but at the same photon energy (3 keV). The foil-stack parameters are as follows: (a) $\theta_r = 1$ mrad, $l_2 = 6$ μm, $l_1 = 106$ μm, $M = 17$; (b) $\theta_r = 2$ mrad, $l_2 = 5.8$ μm, $l_1 = 60$ μm, $M = 18$; (c) $\theta_r = 4$ mrad, $l_2 = 5$ μm, $l_1 = 22$ μm, $M = 21$; (d) $\theta_r = 8$ mrad, $l_2 = 3.2$ μm, $l_1 = 6.2$ μm, $M = 33$. The electron-beam energy is 300 Mev. The distance from the radiator to the detector is 1 m; thus 1 mm represents 1 mrad on the x axis.

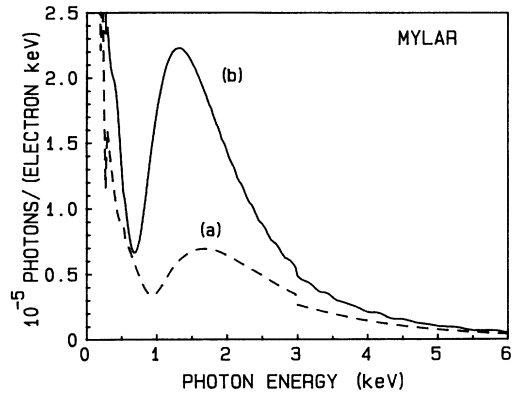

FIG. 7. The calculated spectral density from two RTR Mylar-foil radiators. The radiators were used in the experimental program. The foil-stack parameters are as follows: (a) $l_2=3.5$ μm, $l_1=4.0$ μm, $M=8$, $E=98$ MeV; (b) $l_2=2.5$ μm, $l_1=35$ μm, $M=4$, $E=171$ MeV.

rameters were used in the experiments. The curves show the radiation to be in the soft-x-ray portion of the spectrum with photon energies between 1 and 3 keV.

For higher numbers of foils the calculated spectra show large variations in the spectral density, resulting in the generation of peaks. Some variation in the spectrum has been observed and used to vary the photon energy of the spectrum [6,7,15]. Spectra obtained using incoherent radiators composed of Mylar have also been observed [15,29]. The calculated spectra of Fig. 7 are comparable to those calculated for incoherent radiators and those measured previously [15,29].

III. POSSIBLE APPLICATIONS

A. Particle identification and energy measurements

1. *Analogous behavior of Cherenkov radiation*

The investigation of resonance transition radiation and the current Cherenkov literature suggest the design of RTR particle detectors that are highly analogous to existing Cherenkov detectors [17–22]. A brief comparison between Cherenkov and transition radiation shows us why this is the case. Both processes produce radiation patterns that are coherent and conical, with an angle dependent upon particle velocity and energy. We can therefore investigate the vast Cherenkov literature for areas where *RTR* detectors would be of use, and where they might make a unique contribution.

2. *Threshold detector*

The possibility of detecting particles with energies above a given value is exploited in the threshold counter [19,21]. The threshold Cherenkov counter detects particles that have a velocity sufficient to produce Cherenkov light in the radiator. The threshold velocity β_t is defined as that velocity corresponding to a Cherenkov angle $\theta_c=0$, so that from the Cherenkov condition, $\cos\theta_c=1/\beta n$, $\beta_t=1/n$, where n is the index of refraction of the medium.

In a similar way, we can define a threshold for the RTR effect. From Eq. (12), we see that we can obtain the charged-particle beam energy by measuring the angle of peak photon emission, θ_R:

$$\frac{1}{\gamma^2}\simeq\frac{2r\lambda}{l}-\theta_r^2-\left[\frac{\omega_0}{\omega}\right]^2 \tag{19}$$

or

$$E=\frac{E_0}{\left[\left[\frac{2r\lambda}{l}\right]-\theta_r^2-\left[\frac{\omega_0}{\omega}\right]^2\right]^{1/2}} \tag{20}$$

where E_0 is the rest energy of the emitting charged particle and $l=l_1+l_2$. The threshold energy that can be measured is given by

$$E_t=\frac{E_0}{\left[\left[\frac{2r\lambda}{l}\right]-\left[\frac{\omega_0}{\omega}\right]^2\right]^{1/2}}\ . \tag{21}$$

As we can see from Eq. (12), the angle of peak photon emission increases with electron-beam energy. Since a number of modes can be emitted, a formula for the angle of emission may seem to be difficult to obtain in a closed-form equation. We can again use our simulation program to obtain the annular-peak positions. However, as can be seen from Fig. 8, the calculated peak-emission angle θ_r ($r=1$ mode) from Eq. (12) matches the simulation reasonably well.

The threshold detector usually measures the onset of emission from the radiator. In a Cherenkov detector this is usually done by focusing the Cherenkov radiation on a photomultiplier. The radiator can be a gas whose pressure can be varied in order to change the threshold ener-

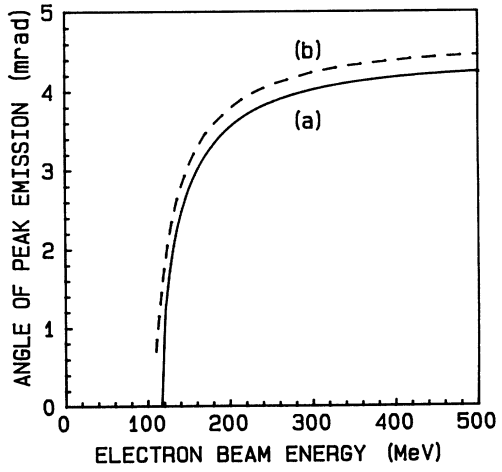

FIG. 8. The calculated angle of peak emission for a resonance foil stack as a function of electron-beam energy. (a) is obtained from Eq. (12), while (b) is a computer simulation of the angular distribution (see examples in Figs. 4 and 5). The radiator contains 36 foils of 5.6-μm Mylar with foil separation of $l_1=16.4$ μm.

gy. A similar device can be constructed using RTR and the $r=m=1$ mode. By selecting proper foil-stack parameters, one can construct a stack to give transition radiation only at charged-particle energies above the threshold energy, $E>E_t$, as given by Eq. (21). A xenon x-ray counter can be used close to the RTR foil stack since we only need to detect the onset of emission. This would make the effect quite useful as a fast electron tagging to supplement the proposed calorimetric identification of electrons in future hadron collider experiments. The simplest RTR arrangement might be a foil stack with parameters chosen so that significant transition radiation is emitted only at energies where the extra electron tagging in would add significantly to the calorimetric information. Since RTR stacks are less than a few centimeters long, they would give a more compact geometry compared to the Cherenkov threshold device, which requires a long container of extremely low-pressure gas in order to operate at superconducting supercollider energies.

Identification of multiple-particle species can be achieved by using more than one foil stack. Several stacks are designed with differing threshold conditions for each particle species. The various foil stacks can be rotated into a beam and the various proportions of species determined. For single-particle identification, alternating stacks (with differing stack parameters) and detectors can be aligned along the particle trajectory for species identification. The efficiency of these stack/detectors must be high—roughly >1 photon per charged particle. This requires alternating identical stacks with detectors.

As an example, we show how one might identify three hadron species in a beam of particles with mean energy of 80 GeV. The threshold and energy differentiation characteristics for three foil stacks and three hadron species (π,k,p) are shown in Fig. 9. Table I gives the three stack characteristics. If stack (a) is in the beam, then all three species will produce RTR. Rotating in stack (b), only kaons and protons emit, while stack (c) would permit only protons to emit. Therefore, measuring the absolute intensity of the flux from these three radiators will give the proportion of hadron species in the beam.

3. *Charged-particle and beam-energy measurements*

For particle energies near the threshold value, the intensity and angle of emission increase rapidly with particle energy. As the particle energy increases, the angle of emission asymptotically approaches the limiting values:

$$\theta_{\max}=\left[\left[\frac{2r\lambda}{l}\right]-\left[\frac{\omega_0}{\omega}\right]^2\right]^{1/2}. \tag{22}$$

The electron-beam energy for θ at 90% of its maximum value is at

$$E_p=\sqrt{10}E_t\ . \tag{23}$$

In the region between E_t and E_p, the measurement of the angle of emission will make an excellent energy detector. In addition, there is a range of energies after E_p before the threshold of the next particle occurs. Particles can therefore be separated and identified in this energy range even though one of the angles of emission has saturated. Again there is an identical phenomenon for the Cherenkov effect which is used in the differential and ring-imaging Cherenkov detector [19,20].

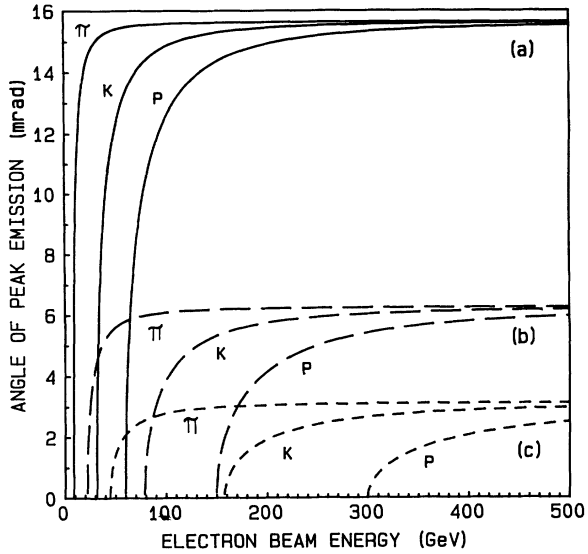

FIG. 9. The calculated angle of peak emission of resonance transition radiation for pions, kaons, and protons. (a) 1.65-μm Mylar foils separated by 3.4 μm. (b) 2.8-μm Mylar foils separated by 21.1 μm. (c) 3.1-μm foils separated by 84.5 μm (see Table I).

Table I and Fig. 9 also give examples of the radiators operating in both the threshold an differential modes. Figure 9 shows both the threshold energies of the three stacks and the angle of peak emission as a function of the

TABLE I. Foil-stack designs for hadron identification.

	Foil stack		
	(a)	(b)	(c)
l_2 (μm)	1.7	2.8	3.1
l_1 (μm)	3.4	21.1	84.5
Δ_1 (μm)	0.5	4.0	16.8
M	10	6	5
	Pions (m_0:139.6 MeV)		
E_t (GeV)	8.9	22.3	44.6
E_p (GeV)	28.3	70.5	141.1
$\theta_{\max}$ (mrad)	15.6	6.3	3.1
	Kaons (m_0:493.7 MeV)		
E_t (GeV)	31.6	78.9	157.8
E_p (GeV)	100.1	249.5	499.0
$\theta_{\max}$ (mrad)	15.6	6.3	3.1
	Protons (m_0:938.3)		
E_t (GeV)	60.1	150.0	300.0
E_p (GeV)	190.2	474.2	948.4
$\theta_{\max}$ (mrad)	15.6	6.3	3.1

energy of the incoming particle. The emission angles for all three particles species increase as a function of energy, saturating at angles of $\theta = 15.6$, 6.3, and 3.1 mrad. For stack (a) the minimum energy for pions is 8.9 GeV.

In the last 15 years, the Cherenkov ring-imaging method has been developed as a way of determining particle energy and direction. Resonance transition radiation might be used in a similar fashion. In the Cherenkov case, the entire Cherenkov ultraviolet radiation cone is imaged. RTR could be imaged in a similar fashion at x-ray frequencies. Following the analysis of Ypsilantis for the ring-imaging Cherenkov detector, one could measure both the particle beam energy and direction [20]. The electron-beam energy would be measured from the angle of peak emission obtained from the ring image (same as the differential counter), while the particle direction would be obtained from the ring-image center.

In order to obtain an accurate image of the x-ray annulus, a 100 or more photon per incident charged particle is needed. Unfortunately, this does not look possible with RTR. Dolgoshein estimates the radiation ability of realistic transition radiators to be extremely low, with the number of x-ray photons limited to $dN/dL \simeq 0.1$ photon/cm, where L is the length of the radiator. From a 10-m-long detector, 100 photons are possible [21]. However, such a long length may produce a prohibitively large number of foils for RTR. In addition, as we can see from Eqs. (17a) and (17b), the foil thickness and spacing would have to be extremely accurate.

However, if there is a sufficient number of particles, the two applications are possible when using RTR in the differential mode. First, one can measure the energy of a charged-particle beam when the current is sufficient for x-ray detection. Such a device would consist of an x-ray detector and foil stack designed to be resonant between E_t and $\sqrt{10}E_t$. This could be used in accelerators to monitor the electron-beam energy without large magnetic spectrometers. The foil-stack radiator could be inserted in the electron beam when a desired energy measurement is needed.

Another possible application would be to determine the proportion of various particle species in a high current beam where there would be adequate x-ray production from the various species. Cherenkov detectors have been used for such a purpose to determine the proportion of various species (e.g., e^- versus π) [23,24]. A RTR detector would be more compact and easily inserted into the beam without major beamline construction. The RTR detector could operate at higher energies than the Cherenkov detector.

We observed RTR in real time with accelerator time structure [10,11]. This allowed us to change electron-beam parameters while observing corresponding changes in x-ray-annular distribution. This flexibility can be important for beam diagnostics and tuning. For example, using the beam diagnostic techniques developed for optical transition radiation by Wartski *et al.* [25] and Rule *et al.* [26], one can determine the emittance of a charged-particle beam. As shown in this paper, the charged-particle beam energy can be obtained by adjusting the foil spacing.

B. Source enhancement

RTR can also be used to increase the spectral brightness (photons per unit solid angle per unit area of source) of a transition-radiation source [14,15,27]. The number of photons is not increased by interfoil coherence; however, since the solid angle of emission can be decreased, the brightness can be increased. We have observed incoherent transition radiation in the soft and in the warm regions of the spectrum [15,28–31]. The brightness of these sources would be greatly enhanced by interfoil coherence.

We have also investigated the use of resonant periodic-dielectric structures for achieving free-electron-laser emission where the electromagnetic wave produced by the periodic-dielectric interacts with the electron beam in a synergistic manner, resulting in the bunching of the electrons and the amplification of the electromagnetic wave [32–34]. The observation of coherent emission for single particles as discussed here increases the possibility that an x-ray free-electron laser utilizing a periodic dielectric may indeed be feasible.

IV. EXPERIMENTAL RESULTS

A. Accelerator selection

Two distinct experimental setups have been used at the linear accelerators at the Naval Postgraduate School (NPS), Monterey, California, and the Saskatchewan Accelerator Laboratory (SAL), University of Saskatchewan, Canada. The NPS linac can give low-current beams ($I < 1$ μA) with energies between 25 and 120 MeV, while the SAL linac gives high-current beams ($I < 50$ μA) with energies between 25 and 300 MeV. Since higher-energy electrons permit the use of larger foil spacing, the SAL accelerator permitted us to design foil stacks with geometries which were easier to construct and required less accurate interfoil spacing.

B. The 90-MeV experiment

Initial experimental work was carried out at the NPS accelerator using radiator stacks designed to generate either coherent or incoherent transition radiation. As shown in Fig. 10, the coherent or RTR stack was made from an assembly of eight concentric steel rings. The rings were cut from steel tubing and ground flat and parallel to the same thickness. Type "C" Mylar (Trademark of E.I. Dupont de Nemours, Inc.) was epoxy bonded to the face of each ring. The smallest Mylar-covered ring was bolted to a flat-ground steel plate. The next larger ring was attached similarly, with the addition of shims between two mating surfaces to space the adjacent Mylar foils by a distance equal to the shim thickness minus the foil thickness. The resonance stack contained eight foils with a nominal foil thickness of 3.5 μm and a nominal foil separation of either 8.5 or 5 μm. Data from the resonance stack were compared to that from an incoherent stack composed of foils of identical thickness and number, but with large, random spacing.

The experimental apparatus shown in Fig. 11 consisted

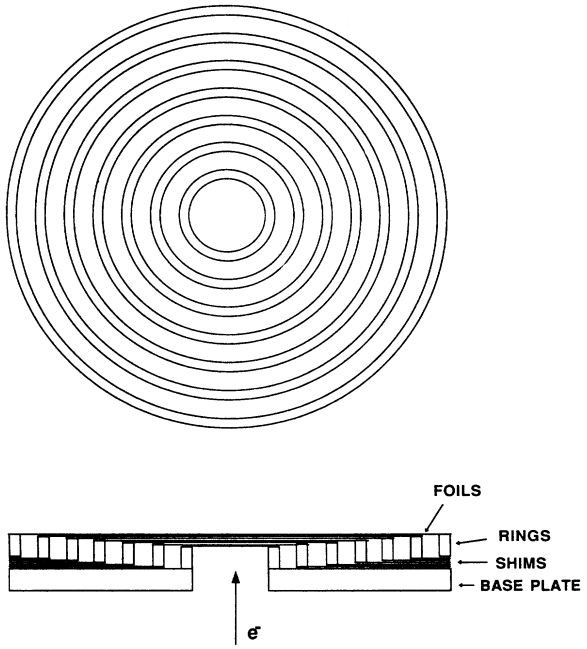

FIG. 10. The RTR Mylar-foil stack composed of an eight-ring stack with three sets of steel shims placed 120° apart. The shims determined the interfoil spacing l_1.

of a foil-stack chamber, dump magnet, and x-ray detector. The foil chamber consists of a 61-cm-diameter vacuum chamber and a target-holder ladder which can be raised and lowered. This allows a phosphor target and up to four stacks to be placed in the electron-beam path without breaking vacuum. The ladder can be rotated around its axis which is perpendicular to the direction of the electrons. This allows the spacing and thickness of the foils to be changed along the direction of the electron path [10]. During the experiment the maximum energy of the accelerator was limited to 97 MeV. The average current was $\simeq 0.1$ μA with a 60-pps repetition rate, and 1-μsec-pulse length.

The angular distribution of soft x rays (1–3 keV) was observed during every machine pulse with a 2.54-cm

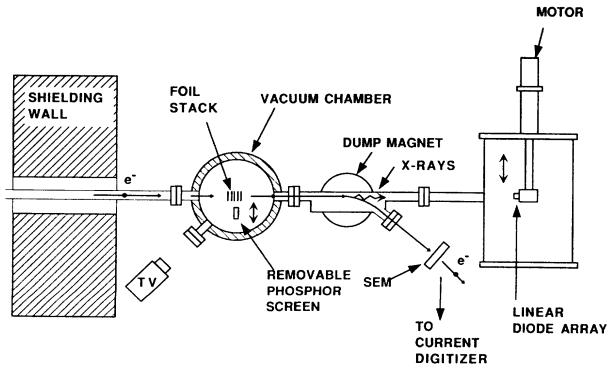

FIG. 11. Monterey NPS experiment. The electron beam enters from the left where it strikes the foil stack and x rays are emitted downstream. The dump magnet separates the electrons from the x rays.

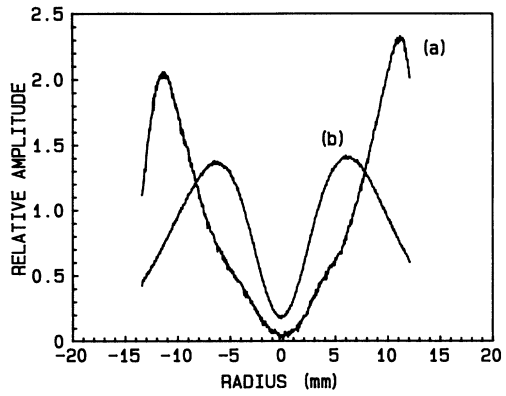

FIG. 12. The measured x-ray spatial distribution for the (a) coherent and (b) incoherent radiators. The coherent radiator consisted of an eight-foil Mylar stack, $l_1 = 8.5$ μm, $l_2 = 3.5$ μm, and the incoherent source consists of eight foils of $l_2 = 3.5$ μm and $l_1 \simeq 1.6$ mm. The electron-beam energy was 98 MeV. The distance from the transition radiator is 1.34 m. In order to match the calculated distribution the l_1 had to be adjusted to 4 μm (see Fig. 3).

linear-diode array (Model No. S2301-512 SPL, windowless version, Hamamatsu Corp.). The array had 512 diodes each, with a photosensitive area 50 μm by 2.5 mm subtending a solid angle of 6.86×10^{-8} sr at the stack-to-detector spacing of 1.34 m. The array could be translated up to 17 cm across and perpendicular to the electron-

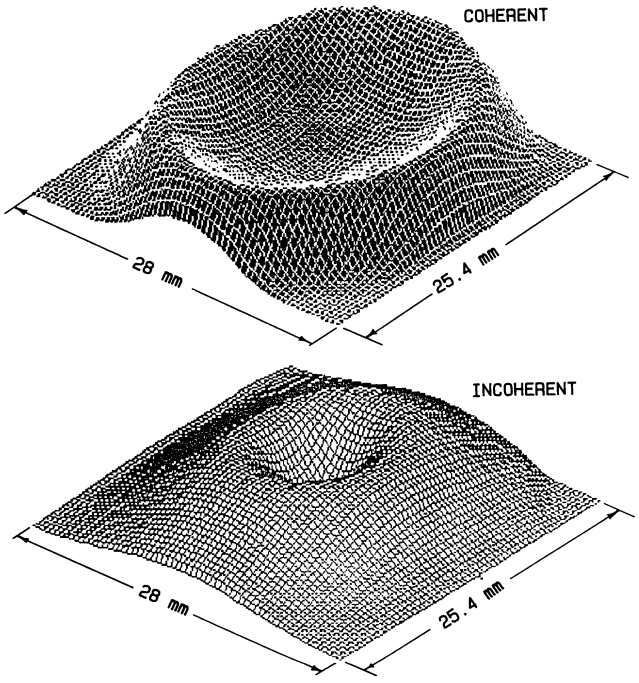

FIG. 13. A fishnet display of the coherent and incoherent x-ray spatial distributions obtained experimentally by scanning the linear-diode array over the x-ray emission cone from incoherent and coherent eight-foil stacks. The same parameters were used as in Fig. 12. See Fig. 19 for a false-color display of annulus at a different electron-beam energy.

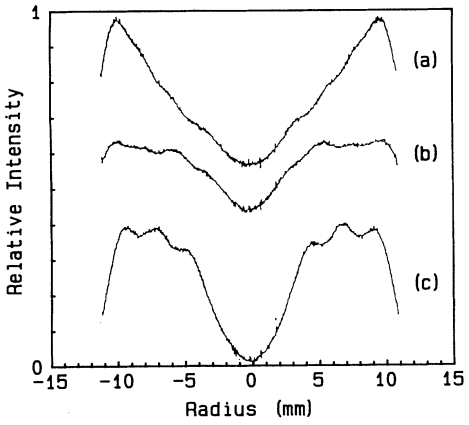

FIG. 14. The spatial distribution for the RTR Mylar-foil stack measured with the linear-diode array and showing interference patterns that varied with time. The radiation pattern was observed to change in time, evolving slowly from pattern (a) to (c) and then jumping quickly back to (a) with no intermediate state. The effect was assumed to be caused by the charging of the foils by the electron beam.

beam axis.

Figure 12 compares typical radiation patterns measured for the incoherent (a) and coherent (b) stacks. The RTR annulus is predicted to be much wider than that generated in the randomly spaced stack. The angle of peak emission for the coherent case is approximately 9 mrad while that of the incoherent case is 4.5 mrad. Translating the diode array across the annulus gives the fishnet plots shown in Fig. 13 for the incoherent and coherent stacks. The angles of peak emission are the same as for Fig. 12. Both the electron-beam energy and foil-stack parameters are the same as in Fig. 12. The figures show that the x-ray resonance cone is symmetrical and much wider than that for the incoherent case. The distribution of the $r=m=1$ RTR mode had the distinctive "cup shape" discussed above, which is quite different from the slow rise and fall of the incoherent mode.

The shape of the angular distribution and the separation of the radiation peaks from the incoherent radiator case agreed with the predicted theoretical values. For the resonance stack, the measured angular separation of the peaks was considerably larger than predicted, being consistent with a foil spacing of 4.0 μm rather than the nomi-

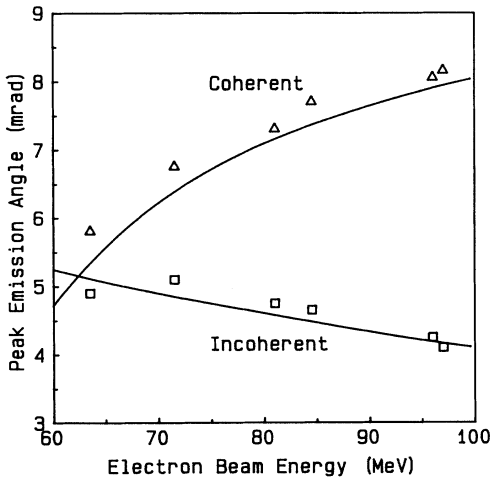

FIG. 15. The measured and calculated peak angle of emission as a function of electron-beam energy. The radiators consisted of eight foils of 3.5-μm-thick Mylar. For the coherent radiator the spacing was designed to be 8.5 μm, for the incoherent radiator 1.6 mm. In order to match the measured results for the coherent radiator, the foil spacing has to be adjusted to $l_1=4$ μm (solid curve). The calculated distribution (solid curve) for the incoherent radiator matched the experimental results. The figure shows the peak-emission angle increases with increasing energy for the coherent radiator, while for the incoherent case, the angle of emission decreases with increased electron-beam energy.

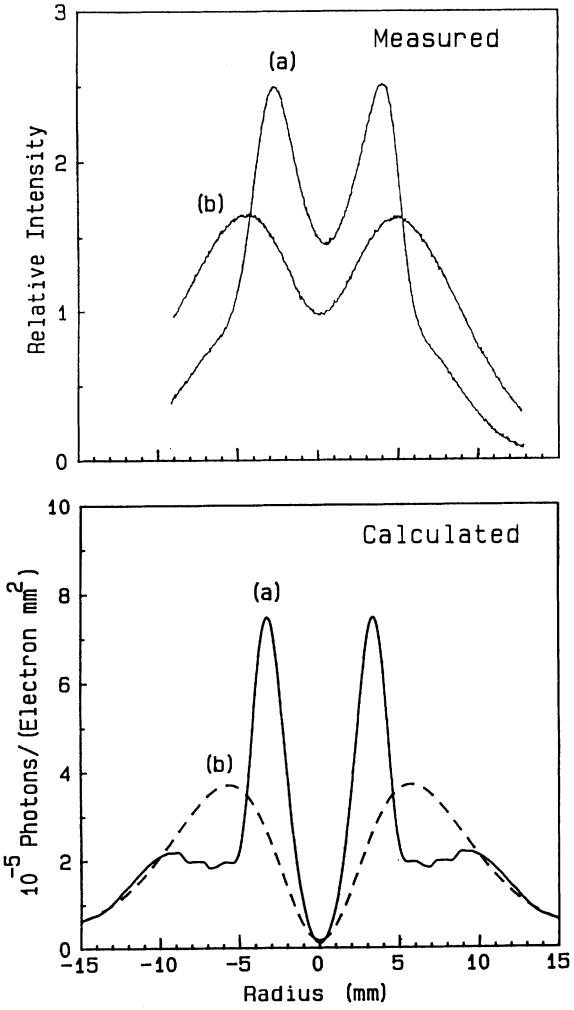

FIG. 16. The measured (top) and calculated (bottom) spatial distribution for the (a) coherent eight-foil Mylar stack and (b) incoherent foil stack. The electron-beam energy was $E=93$ MeV. Mylar foils were of thickness $l_2=3.5$ μm, and spacing $l_1=5$ μm for the coherent stack and $l_1\simeq 1.6$ mm for the incoherent stack. In order to match the observed peak-to-peak spatial distribution, l_1 had to be adjusted to 17 μm. As demonstrated theoretically in Fig. 6, this figure shows experimentally that the ring-image pattern can be made smaller than the $\theta=1/\gamma$ incoherent emission pattern. The distance from the stack of the radiator was 1.34 m.

nal spacing of 8.5 μm. Comparing Fig. 12 with the calculated distribution of Fig. 3 where we have adjusted l_1 to be 4 μm, we find that the measured RTR modes match the predicted spatial distributions.

The change in spacing might be due to electrostatic forces between the very closely spaced foils caused by surface charge accumulation. The angular distribution of the x-ray emission from the coherent stack was found to oscillate between three distinct radiation patterns as shown in Fig. 14. The period of evolution from 14(a) to 14(c) varied between 10 and 45 sec and might be explained by gradual electrostatic charging of the foils by the electron beam. The rapid change back from 14(c) to 14(a) (less than 0.5 sec with no intermediate mode) is consistent with discharging of the foils. In subsequent experiments discussed below, aluminized-Mylar foils were used to drain the accumulated surface charges and a single angular mode was observed. As one would expect, the incoherent mode showed no such variation.

Despite this difficulty, we have obtained clear experimental evidence of energy determination using the resonance stack. The experimental values for the coherent and incoherent stacks are plotted in Fig. 15. The experimental values for the two cases were obtained at the same energies and sequentially. For the coherent stack, Fig. 15 shows the experimental values to be much larger than the predicted ones for the values of $l_1 = 8.5$ μm and $l_2 = 3.5$ μm. If we adjust l_1 to be 4.0 μm, the theoretical predictions match the experimental values. Note that as the electron-beam energy increases from 63 to 97 MeV, the angle of peak emission decreases for the incoherent stack, and increases for the coherent stack. For the incoherent stack, Fig. 15 shows the experimental values to be very close to the predicted ones. Thus the angle of peak emission, θ_r, of the coherent radiator obeys Eq. (11) while that of the incoherent radiator obeys Eq. (4a).

In order to improve the spacing, the eight-foil Mylar stack was reshimmed to give a spacing of 5 μm between foils with l_2 again equal to 3.5 μm. The x-ray spatial distribution was again measured and compared with an incoherent foil stack. Unfortunately, as before, the calculated peak-to-peak spatial distribution was not the same as the measured distribution. In order to match the peak-to-peak spatial distribution, l_1 had to be adjusted to 17 μm. These measured and calculated spatial distributions for the (a) coherent and (b) incoherent radiators are shown in Fig. 16. The large discrepancy in interfoil spacing can only be attributed to the mechanical method of spacing the foils.

Note that the peak-to-peak separation is now less than the $1/\gamma$ separation of the incoherent stack, exactly opposite to the previous measurements. Thus the experiment showed that the radiation cone from the coherent radiator could be collapsed below the $1/\gamma$ cone angle as predicted by Fig. 6. This is important for increasing the intensity of the x-ray flux by making the source more collimated.

C. The 200-MeV experiment

In order to make the foil spacing large enough so that mechanical tolerances on spacing could be relaxed, we decided to go to a higher electron-beam energy and reduce the number of foils. From Eqs. (1) and (10) one can see that a RTR stack matched to a higher beam ener-

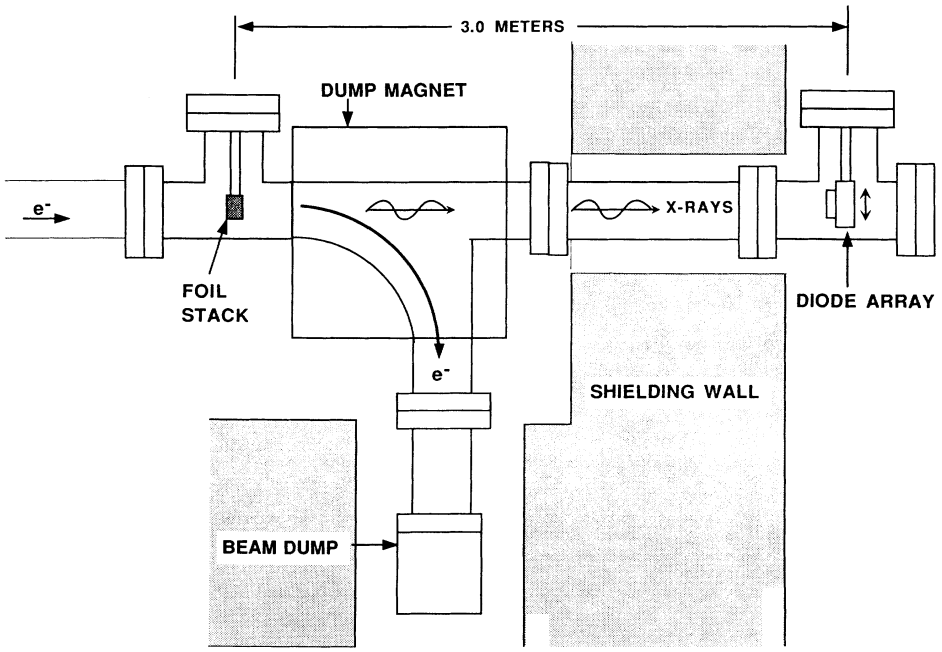

FIG. 17. Experimental apparatus for measuring the spatial distribution of transition radiation at $\simeq$200 MeV. The electron beam enters from the left where is strikes the foil stack and x rays are emitted downstream. The dump magnet separates the electrons from the x rays. The detector is a Hamamatsu linear-diode array.

gy will have a larger foil spacing. From Eq. (17a) we also note that the longitudinal error on the foil thickness can be larger, still permitting x-ray phase addition between the foils. Thus the foil stacks were easier to fabricate and compare to the theoretical predictions.

Since the NPS linac was limited to 100 MeV, we decided to use the SAL linac. The apparatus at this accelerator, shown in Fig. 17, was almost identical to that of the NPS accelerator. We utilized an existing vacuum chamber for the transition radiators, a 90°-bending magnet for separating the electrons from the photons, and an 8-foot shaft in the floor for dumping the electrons.

The experiments used diode arrays which could scan the entire x-ray cone. Two targets were constructed using 2.5-μm aluminized Mylar. Each target consisted of four foils with either 35-μm or 48-μm spacing. The number of foils was limited because of the size of the existing target vacuum chamber. These targets are similar to the eight-foil coherent radiator of the NPS experiments. Aluminizing the foils eliminated the time-dependent variation in foil spacing due to electrostatic forces.

The observed radiation pattern again showed that phase addition was occurring at angles larger than $1/\gamma$. The pattern differed from the NPS measurements in that the radiation intensity was not of equal intensity around the annulus. An example of the RTR annulus for the $l_1 = 35$-μm stack is shown as a fishnet plot in Fig. 18. As one might predict from Fig. 5, the four-foil stack does not give as clear an image as did the eight-foil resonance stack.

Obtaining a completely symmetrical annulus was difficult. As shown in Fig. 19(a) for the $l_1 = 48$ μm stack, the asymmetry of the mode is shown more clearly using a false-color display of the measured x-ray emission. These displays [Figs. 19(a) and 19(b)] were obtained as were the fishnet plots, by scanning the diode array across the x-ray annulus at a distance of 3 m from the radiator. The color scale starts with red as the most intense, and goes through the color spectrum to blue and black as the least intense. Areas of high intensity or "hot spots" were ob-

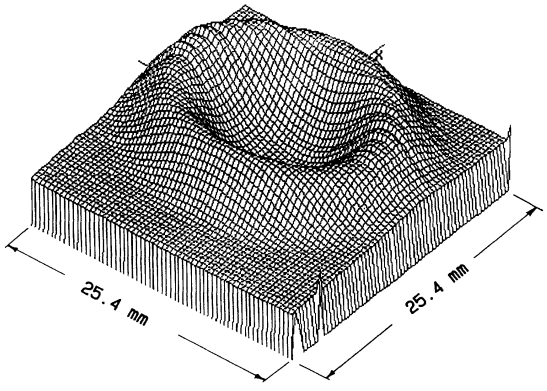

FIG. 18. A three-dimensional display of the measured soft-x-ray emission from the four-foil resonant stack. The foil thickness and spacing is $l_2 = 2.5$ μm and $l_1 = 35$ μm. The electron-beam energy was 171 MeV. The distance from the stack to the radiator was 3 m.

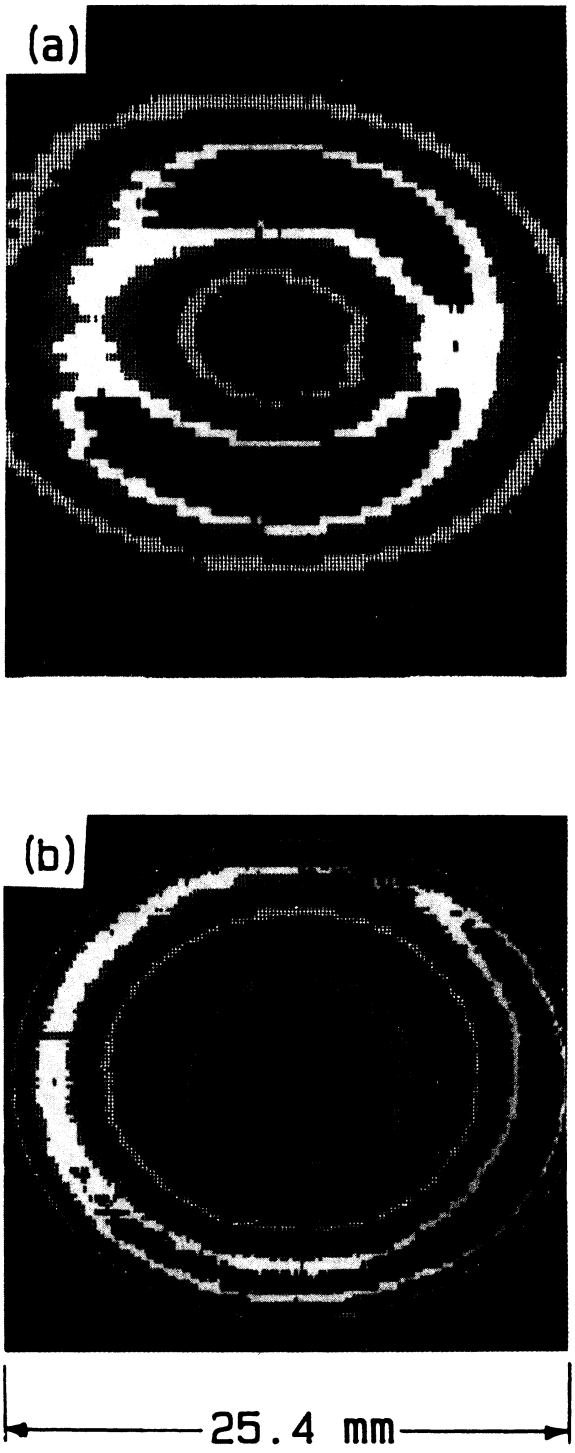

FIG. 19. (a) A false-color display of the measured soft x rays from the four-foil RTR stack. The radiator was composed of $l_2 = 2.5$ μm and $l_1 = 48$ μm. The electron-beam energy was 170 MeV obtained from the SAL accelerator. Distance from the foil stack to the detector is 3 m. (b) A false-color display of the measured soft x rays from the eight-foil RTR stack. The electron-beam energy was 94.3 MeV obtained from the NPS accelerator. The parameters of the stack are given in Fig. 12. The color scale starts with red as the most intense, going through the spectrum to blue and black as the least intense.

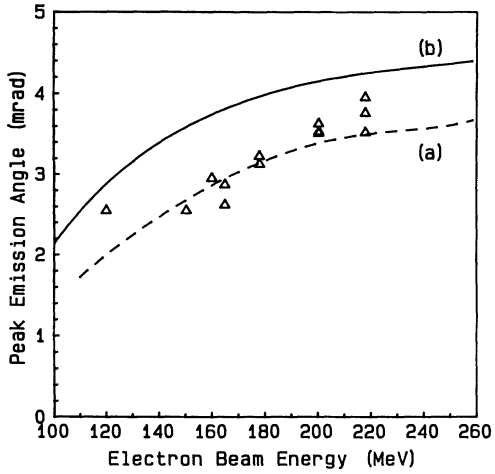

FIG. 20. The measured and calculated peak angle of emission as a function of electron-beam energy. The coherent radiator is a four-foil stack with $l_2=2.5$ μm, $l_1=35$ μm. The calculated values for $l_1=48$ μm (a) and $l_1=35$ μm (b) are given, showing that the 48-μm spacing was closer to the measured values.

served at points diametrically opposite one another, indicating that most of the phase addition was at these points. This effect is believed to be due to the electron-beam-spot shape and divergence (beam emittance). The electron-beam energy was 171 MeV.

If we compare this example with that obtained from the eight-foil stack at NPS shown in Fig. 19(b), we find that the annulus from the eight-foil stack is more well defined because of the larger number of foils. In addition the annulus is more symmetrical, with only a small amount of asymmetry at the lower right of the figure. The control of the electron beam at the target area of the NPS accelerator was somewhat better than that at the SAL accelerator. These displays indicate that RTR can be used to determine the emittance of the electron beam as discussed previously [10,11,25,26].

As with the resonance experiments at NPS, the angle of peak emission increased with electron-beam energy, indicating that we were again observing coherent emission. Unlike the NPS experiments, no incoherent stack was used because the small target vacuum chamber could only hold one target at a time. The variation of peak-emission angle as a function of electron-beam energy is given in Fig. 20.

The calculated angle of peak emission is shown in Fig. 20 for both the (a) $l_1=48$ and (b) $l_1=35$ μm cases. The spatial distribution for the 48-μm spacing appears to match the experimental data more accurately. Although the measured peak angle is again smaller than the calculated angle, the percent difference is not as large as the eight-foil stack used in the lower-electron-beam-energy experiments at NPS.

The variation in the angle of peak emission for particular beam energies can be attributed to changes in beam divergence, direction, and area between measurements. We had some difficulty in determining the electron beam's size and divergence because there was no phosphor screen down-stream from the radiator, and the upstream screen was too far away to be of much service in determining the beam quality near the radiator.

V. CONCLUSIONS

The experimental results show that we are observing interfoil coherence and that the location of the angular peaks can be changed with foil spacing, foil thickness, and charged-particle energy. In the field of high-energy physics, these results might be important for particle detection and for beam diagnostics. As an x-ray source, the resonance effect can increase the brightness of the source and free-electron-laser action may be possible.

Using RTR in either the threshold or differential mode appears to be most feasible for species identification in charged-particle beams of moderate current. Identification of single charged particles does not appear to be feasible for the ring-image RTR detector because the total number of x-ray photons is not adequate for ring resolution. Fewer that 100 photons per charged particle can be generated from a foil stack. Alternating stacks and detectors can increase the sensitivity of the RTR threshold detector so that single charged particles can be identified.

Designing the radiator to have peak emission for the $r=m=1$ mode gives the highest annulus definition. In addition, the peak can be adjusted over a range of emission angles which are greater or less than $1/\gamma$, the angle of maximum emission for a single interface. The range of angles is limited to $0<\theta_r<\theta_m$. Designing the radiator to emit at $\theta_1\simeq 1/\gamma$ gives the maximum peak photon flux. For moderate-energy charged particles, designing the radiators to emit at angles greater than $1/\gamma$ may permit the separation of the x rays from the emitting charged particles without magnetic fields.

Our difficulties in matching precisely the calculated and measured spatial distributions at these electron-beam energies are somewhat disconcerting. Going to higher electron-beam energies, as we did at the SAL experiments, appears to have helped remedy the situation. Going to still higher electron-beam energies as was done by Goedtkindt *et al.* and Vorob'ev *et al.*, achieved more precise results [12,35]. Other, more accurate, methods of achieving interfoil spacing should also improve the results.

ACKNOWLEDGMENTS

This work was supported by the Department of Energy under the Small Business Innovative Research (SBIR) program, Grant Number DE-AC03-86ER80428, Canadian Natural Science and Engineering Research Council (NSERC), and the Naval Postgraduate School.

[1] V. L. Ginzburg and I. M. Frank, J. Phys. (Moscow) **9**, 353 (1945).
[2] G. M. Garibyan, Zh. Eksp. Teor. Fiz. **33**, 1403 (1958) [Sov. Phys.—JETP **6**, 1079 (1958)].
[3] M. L. Ter-Mikaelian, Nucl. Phys. **24**, 43 (1961).
[4] C. W. Fabjan and W. Struczinski, Phys. Lett. **57B**, 483 (1975).
[5] M. L. Cherry and D. Müller, Phys. Rev. Lett. **38**, 5 (1977).
[6] A. N. Chu, M. A. Piestrup, P. F. Finman, R. H. Pantell, and R. A. Gearhart, IEEE Trans. Nucl. Sci. **NS-29**, 336 (1982).
[7] P. F. Finman, M. A. Piestrup, P. H. Pantell, and R. A. Gearhart, IEEE Trans. Nucl. Sci. **NS-29**, 340 (1982).
[8] P. J. Ebert, M. J. Moran, B. A. Dahling, B. L. Berman, M. A. Piestrup, J. O. Kephart, H. Park, R. K. Klein, and R. H. Pantell, Phys. Rev. Lett. **54**, 893 (1985).
[9] M. J. Moran, B. A. Dahling, P. J. Ebert, M. A. Piestrup, B. L. Berman, and J. O. Kephart, Phys. Rev. Lett. **57**, 1223 (1986).
[10] M. A. Piestrup, D. G. Boyers, Qiang Li, M. J. Moran, F. R. Buskirk, R. M. Robinson, X. K. Maruyama, J. R. Neighbors, and D. D. Snyder, IEEE Trans. Nucl. Sci. **NS-35**, 464 (1988).
[11] M. A. Piestrup, D. G. Boyers, C. I. Pincus, Qiang Li, M. J. Moran, J. C. Bergstrom, H. S. Caplan, R. M. Silzer, D. M. Skopik, X. K. Maruyama, F. R. Buskirk, J. R. Neighbors, and G. B. Rothbart, Nucl. Instrum. Methods B **40/41**, 965 (1989).
[12] P. Goedtkindt, J. M. Salome, X. Artu, P. Dhez, M. Jablonka, N. Maene, F. Poortmans, and L. Wartski, Nucl. Instrum. Methods B **56-57**, 1060 (1991).
[13] M. L. Cherry, G. Hartman, D. Muller, and T. A. Prince, Phys. Rev. D **10**, 3594 (1974).
[14] A. N. Chu, M. A. Piestrup, T. W. Barbee, Jr., and R. H. Pantell, J. Appl. Phys. **51**, 1290 (1980).
[15] M. A. Piestrup, P. F. Finman, A. N. Chu, T. W. Barbee, Jr., R. H. Pantell, R. A. Gearhart, and F. R. Buskirk, IEEE J. Quantum Electron. **QE-19**, 1771 (1983).
[16] G. M. Garibyan, L. A. Gerorgyan, and C. Yang, Zh. Eksp. Teor. Fiz. **66**, 552 (1974) [Sov. Phys.—JETP **39**, 265 (1974)].
[17] J. Litt and R. Meunier, Annu. Rev. Nucl. Sci. **23**, 1 (1972).
[18] J. Seguinot and T. Ypsilantis, Nucl. Instrum. Methods. **142**, 377 (1977).
[19] P. Lecomte, G. Poelz, R. Riethmüller, O. Römer, and P. Schmüser, Phys. Scr. **23**, 377 (1981).
[20] T. Ypsilantis, Phys. Scr. **23**, 371 (1981).
[21] B. Dolgoshein, Nucl. Instrum. Methods A **252**, 137 (1986).
[22] J. P. Stroot, Nucl. Instrum. Methods A **248**, 103 (1986).
[23] A. I. Alichanizn, V. I. Baskakov, V. K. Chernjatin, B. A. Dolgoshein, V. M. Fedorov, I. L. Gavrilenko, S. P. Konovlov, O. M. Kozodaeva, V. N. Lebedenko, S. N. Majburov, S. V. Muravjev, V. P. Pustoventov, A. S. Romanjuk, A. P. Shemeleva, and P. S. Vasiljev, Nucl. Instrum. Methods **158**, 137 (1979).
[24] M. Deutschmann, W. Struczinski, C. W. Fabjan, W. Willis, I. Gavrilenko, S. Maiburov, A. Schmeleva, P. Vasiljev, V. Tchernyatin, B. Dolgoshein, V. Kantserov. P. Nevski, and A. Sumarkov, Nucl. Instrum Methods **180**, 409 (1981).
[25] L. Wartski, S. Roland, J. Lasalle, M. Bolore, and G. Filippi, J. Appl. Phys. **46**, 3644 (1976).
[26] D. W. Rule, R. B. Fiorito, A. H. Lumpkin, R. B. Feldman, and B. E. Carlsten, Nucl. Instrum. Methods A **296**, 739 (1990).
[27] M. J. Moran, Nucl. Instrum. Methods B **33**, 18 (1988).
[28] M. A. Piestrup and M. J. Moran, Appl. Phys. Lett. **50**, 1421 (1990).
[29] M. A. Piestrup, J. O. Kephart, H. Park, R. K. Klein, R. H. Pantell, P. J. Ebert, M. J. Moran, B. A. Dahling, and B. L. Berman, Phys. Rev. A **32**, 917 (1985).
[30] M. A. Piestrup, M. J. Moran, D. G. Boyers, C. I. Pincus, J. O. Kephart, R. A. Gearhart, and X. K. Maruyama, Phys. Rev. A **43**, 2387 (1991).
[31] M. A. Piestrup, D. G. Boyers, C. I. Pincus, J. L. Harris, R. M. Silzer, D. M. Skopik, and X. K. Maruyama, Phys. Rev. A **43**, 3653 (1991).
[32] M. A. Piestrup and P. F. Finman, IEEE J. Quantum Electron. **QE-19**, 389 (1983).
[33] M. A. Piestrup, IEEE J. Quantum Electron. **QE-24**, 591 (1988).
[34] M. B. Reid and M. A. Piestrup, IEEE J. Quantum Electron. **QE-27**, 2455 (1991).
[35] S. A. Vorob'ev, V. N. Zabaev, V. V. Kaplin, B. N. Kalinin, A. P. Potylitsyn, E. I. Rozum, and S. R. Uglov, Pis'ma Zh. Eksp. Teor. Fiz. **53**, 332 (1991) [Sov. Phys.–JETP Lett. **53**, 332 (1991)].

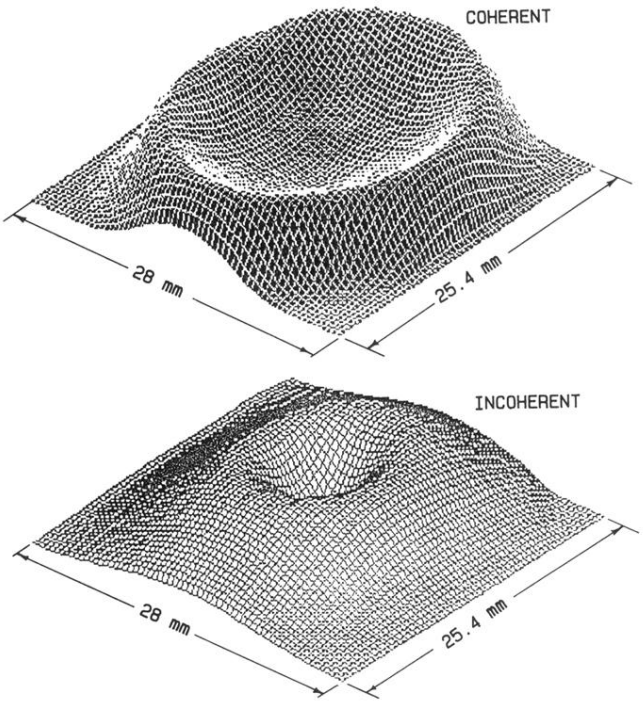

FIG. 13. A fishnet display of the coherent and incoherent x-ray spatial distributions obtained experimentally by scanning the linear-diode array over the x-ray emission cone from incoherent and coherent eight-foil stacks. The same parameters were used as in Fig. 12. See Fig. 19 for a false-color display of annulus at a different electron-beam energy.

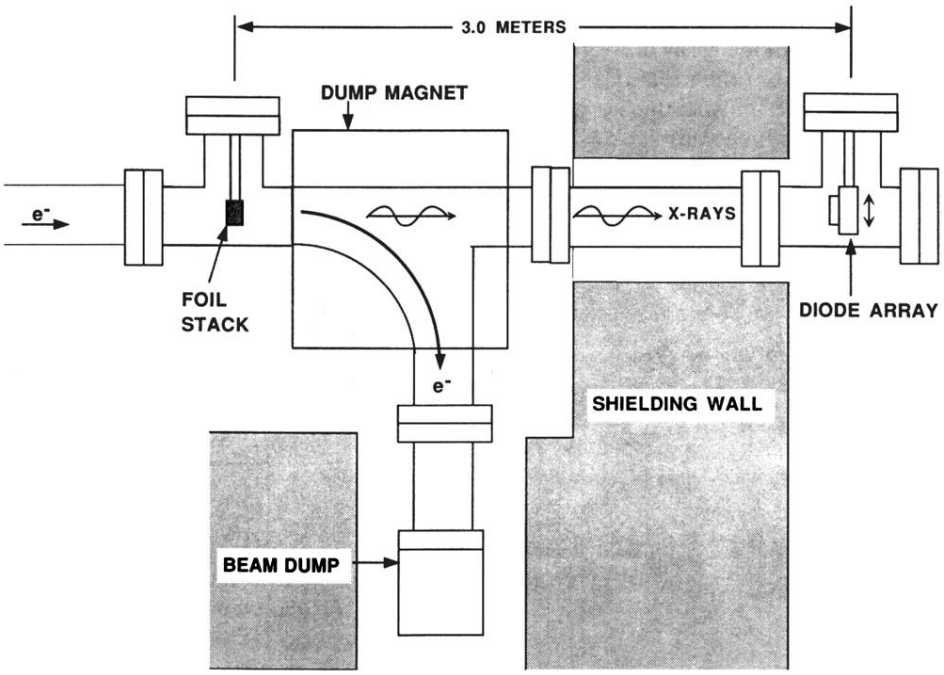

FIG. 17. Experimental apparatus for measuring the spatial distribution of transition radiation at $\simeq 200$ MeV. The electron beam enters from the left where is strikes the foil stack and x rays are emitted downstream. The dump magnet separates the electrons from the x rays. The detector is a Hamamatsu linear-diode array.

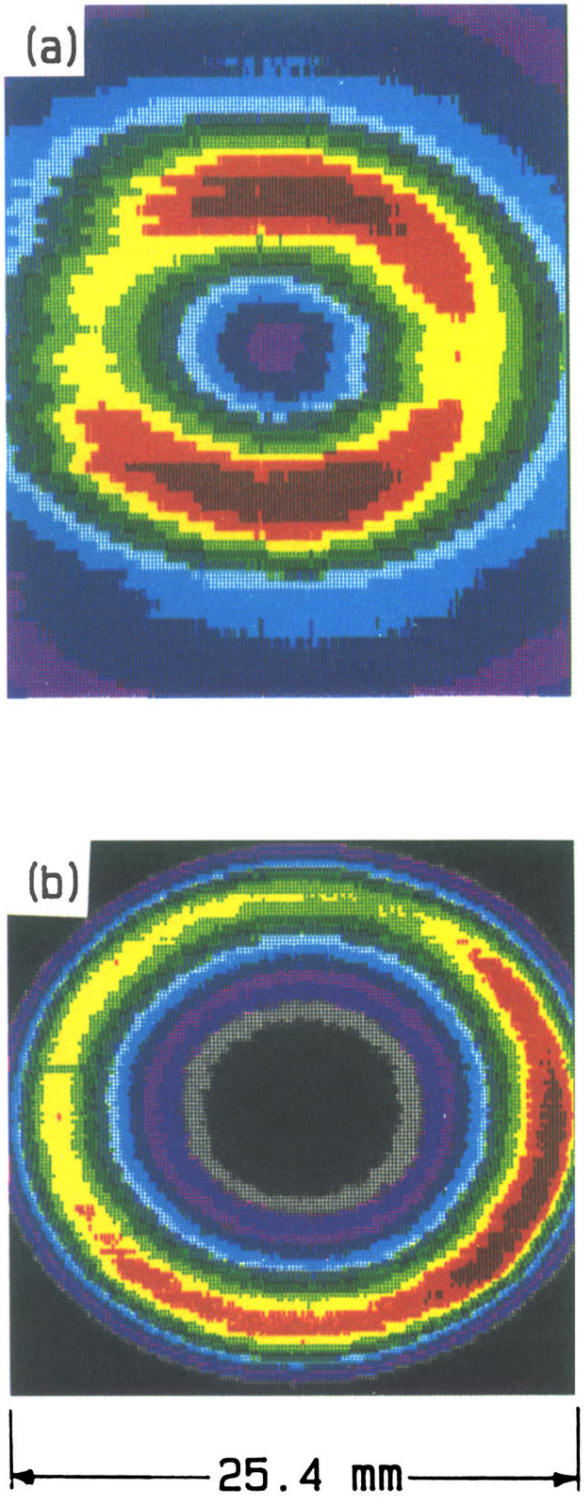

FIG. 19. (a) A false-color display of the measured soft x rays from the four-foil RTR stack. The radiator was composed of $l_2 = 2.5$ μm and $l_1 = 48$ μm. The electron-beam energy was 170 MeV obtained from the SAL accelerator. Distance from the foil stack to the detector is 3 m. (b) A false-color display of the measured soft x rays from the eight-foil RTR stack. The electron-beam energy was 94.3 MeV obtained from the NPS accelerator. The parameters of the stack are given in Fig. 12. The color scale starts with red as the most intense, going through the spectrum to blue and black as the least intense.

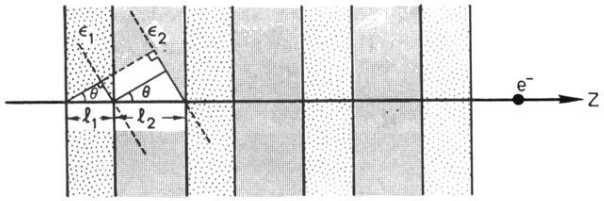

FIG. 2. Resonance transition radiation from a periodic medium with uniform spacing. If the phase velocity of the emitted radiation along the z direction slips out of phase by $2\pi r$ rad (r is an integer) for each foil pair interface, the radiation adds in phase and the intensity varies as square of the number of foils.